Smart Structures and Systems, *Vol. 28, No. 4 (2021) 443-453*
https://doi.org/10.12989/sss.2021.28.4.443

A corrosion threshold-controllable sensing system of Fe-C coated long period fiber gratings for life-cycle mass loss measurement of steel bars with strain and temperature compensation

Chuanrui Guo and Genda Chen*

Department of Civil, Architectural and Environmental Engineering, Missouri University of Science and Technology, Rolla, MO 65401, USA

(*Received May 21, 2020, Revised March 31, 2021, Accepted July 6, 2021*)

Abstract. In this study, a corrosion threshold-controllable sensing system of long period fiber gratings (LPFG) is developed and validated for life-cycle monitoring of steel bars in corrosive environments. Three Fe-C coated LPFG sensors with two bare LPFG sensors in LP_{06} and LP_{07} modes for strain and temperature compensation were multiplexed and deployed inside three miniature, coaxial steel tubes to measure three (long-term in years) critical mass losses through the penetration of tube walls and their corresponding (short-term in hours) corrosion rates in the life span of steel bars. The strain/temperature and mass loss measurements are based on the changes in grating period and refractive index of surrounding medium, respectively. Thermal/mechanical loading and accelerated corrosion tests were conducted to validate the functionality, sensitivity, accuracy, and robustness of the proposed sensing system. Since both the steel tube and Fe-C layer represent the material composition of steel bars in the context of corrosion, the mass loss correlation among any two of the steel tube, Fe-C layer and steel bar is independent of the test conditions such as the current density and sample length, and thus applicable to engineering practices. The outer tube can notably delay and decelerate the corrosion process of its inner steel tube due to the reduced current effect.

Keywords: corrosion monitoring; long period fiber gratings; sensitivity; sensor packaging; service life

1. Introduction

In structural health monitoring, strain is one of the most important parameters to measure in engineering applications (Deng and Cai 2007, Deng *et al*. 2019). It can provide essential information about the rebar performance condition, concrete crack indication and behavior of steel members. Temperature is another parameter that affects the structural performance and must be compensated for strain measurement during seasonal fluctuations or extreme conditions such as fire and explosion. For strain monitoring, the most commonly used technique is the strain gauge that utilizes the correlation between the deformation of a metallic foil and its electrical resistance. For in-situ applications, this technique has several drawbacks. First, the thermal expansion on a strain gauge induced by temperature change is detected as strain, thus compounding the measurement of mechanical strain. To address this issue, self-compensated strain gauges have been developed by using an alloy with the same coefficient of thermal expansion (CTE) as that of the metal specimen to be tested. Another method is to install a dummy gauge on an unstrained portion of the same specimen. In this case, the readout from the dummy gauge is only the thermal induced deformation, which can be used to compensate the temperature effect in a nearby strain gauge. This method requires an extra step of the test setup for an unstrained sample in the tested area. Second, voltage applied to the electrical circuits (from which the change in electrical resistance is measured) must be small (mV or even μV) enough to control the generated heat. Any amplification effect of the heat during the measurement process may lead to additional noise. For example, the associated electromagnetic interference (EMI) affects the quality of signals, depending on their intensity level. Third, when not installed with protection from surrounding moisture, the strain gauge wire will be corroded over time and thus the output signal will not be accurate. Currently, epoxy and polymer have been widely used to protect the strain gauge from corrosion during long-term measurement. In the cases of high temperature, debonding, and high intensity chemical invasive environment, the strain gauge is still fragile since the insulation material cannot provide sufficient protection.

For temperature measurement, many techniques have been developed (Bhatia *et al*. 1996, Mizuno *et al*. 2015, Urrutia *et al*. 2016, Wen *et al*. 2015, Zhao *et al*. 2016). One of the most popular sensors is thermal coupler. As an electrical device, a thermocouple consists of two dissimilar electrical conductors and forms electrical junctions at differing temperatures. A thermocouple produces a temperature-dependent voltage as a result of the thermoelectric effect, which can be calibrated with the applied temperature. The range in temperature measurement of a thermocouple is typically from 200°C to 2600°C with a short response time. On the other hand, attention must be paid to several disadvantages. First, since the material used

*Corresponding author, Professor,
E-mail: gchen@mst.edu

ISSN: 1738-1584 (Print), 1738-1991 (Online)

in thermocouples is metal, corrosion will be a potential long-term concern. Once occurred, corrosion will lead to erroneous readings of the thermocouples. Second, to provide accurate results, thermocouples must be recalibrated within a specific period of time after each usage, which is difficult for continuous monitoring and time consuming in practice. Third, similar to the strain gauges, thermocouples are vulnerable to EMI with increasing measurement errors.

To address the above issues associated with both strain and temperature measurements, fiber optic sensors (FOS) have been proposed, developed and tested in the past decades (Deng and Cai 2007, Leng and Asundi 2003, Wang *et al*. 2010, Xu *et al*. 2012). Compared to the strain gauges and thermocouples, the FOS have several unique advantages in structural health monitoring: 1) a compact optic fiber with hundreds of microns in diameter requires less space or room for installation, 2) the fiber made of silica is immune to the EMI effect, 3) silica fibers can stand temperature up to 1,000°C after annealing (Bao and Chen 2016) and high temperature resistant fibers and sapphire fibers can work under much higher temperatures (Wang *et al*. 2010), 4) due to the silica material, the FOS are not affected by the corrosive environment such as moisture, oxidization and chemical invasive circumstance, and 5) the FOS have low attenuation loss over a long distance in kilometers in applications for in-situ tests. Even though the FOS are advantageous over the traditional methods, a bare fiber is too fragile to survive the brutal action during installation and application. Extra protection is required of fiber grating sensors such as LPFG and fiber Bragg gratings (FBG).

Corrosion is a natural process that gradually destructs metal through electrochemical reaction with its environment. The reaction gradually converts the metal into a chemically stable form, such as oxide, hydroxide and sulfide, which undermines its mechanical strength (Chen *et al*. 2015, Panossian *et al*. 2012). In civil engineering, structures are often exposed to the environment that accelerates the corrosion process of steel rebar (Zaki *et al*. 2015): 1) deicing salt, seawater and moisture to form electrolytes for electrochemical reactions; 2) chloride ion, CO_2 and sulfur contamination from the atmosphere to destroy the passivation film formed on the rebar surface; and 3) tension stress/fatigue induced cracks that increase the contact area and penetration depth during the corrosion process. Compared to the indirect parameters that can be obtained from conventional corrosion monitoring techniques, such as visual inspection, open circuit potential (OCP) and resistance (Figueira 2017, Zaki *et al*. 2015), corrosion-induced mass loss is a more direct parameter that can provide engineers with critical data in their decision making for maintenance strategy development (Chen *et al*. 2016). Mass loss measurement can also help understand how the corrosion process develops, which will enhance the corrosion prevention and protection design of metal structures.

In our previous work, Fe-C coated LPFG corrosion sensors have been systematically studied for mass loss measurement using accelerated corrosion tests under strain-free conditions in laboratory (Chen *et al*. 2016, Guo *et al*. 2019, Huang *et al*. 2013). For in-situ applications, the corrosion process is compounded by the strain induced by traffic and extreme loads, and the daily/seasonal change in temperature. Indeed, the effect of strains on the corrosion behavior of Fe-C layers must be taken into account as demonstrated in Guo *et al*. (2020). Furthermore, the slow process of corrosion takes years. The sensors can provide mass loss measurement for approximately 60 hours at zero strain and 30 hours at a strain of 1500 με. Therefore, considering the effects of strain and temperature and increasing the service life of the Fe-C coated LPFG sensors are essential to bringing the sensor technology into applications for long-term monitoring of steel structures.

In this study, an integrated sensing system is proposed, designed and tested for a simultaneous measurement of strain, temperature, and corrosion-induced mass loss in long term. The system consists of three coaxial steel tubes in different diameters and five LPFG sensors. Two LPFG sensors in LP_{06} and LP_{07} modes are utilized for strain and temperature measurements. Three Fe-C coated LPFG sensors are designed for corrosion induced mass loss measurement. Both the steel tubes and the Fe-C coating compositions represent the material of steel members or structures to be monitored, all of them experiencing the same corrosion process over time. The three steel tubes can not only protect the inside LPFG sensors from external mechanical impact, but also provide three corrosion thresholds (in the order of years) in practical applications and enable the long–term monitoring of corrosion for life-cycle assessment of steel structures. The integration of multiple LPFG sensors allows a discrimination of strain, temperature and mass loss.

2. Sensor design

2.1 LPFG sensors

A LPFG sensor is an optical device with the refractive index of its fiber core modulated periodically in hundreds of microns (Vengsarkar *et al*. 1996). Due to its long period in comparison with the wavelength of radiation propagating in the fiber, the LPFG couples the fundamental mode of the fiber core into the cladding mode and thus generates a series of attenuation bands due to the energy dissipation from the coupled cladding mode into the surrounding medium. The wavelength at each attenuation band is defined as the resonant wavelength λ_{res} and it can be obtained by the couple mode theory (Erdogan 1997, Vengsarkar *et al*. 1996)

$$\lambda_{res} = (n_{eff}^{co} - n_{eff}^{cl,0j})\Lambda \quad (1)$$

where n_{eff}^{co} is the effective refractive index of the core, $n_{eff}^{cl,0j}$ is the effective refractive index of the j^{th} order ($j > 1$) cladding mode and is partially determined by the refractive index of the surrounding medium, and Λ is the grating period. The grating period is responsive to any strain and temperature applied on the fiber, and the refractive index is adaptive to the environment surrounding the fiber in applications. Therefore, while FBG sensors can be used to

measure strain and temperature only, LPFG sensors have unique capability of sensing the change in refractive index of its surrounding medium, such as corrosion applications in metal structures.

An electromagnetic wave propagates along the LPFG inscribed on a single-mode optical fiber in hundreds of linearly polarized (LP) modes (Gloge 1971, Snyder 1969). For convenience, the j^{th} order cladding mode is referred to as the LP_{0j} mode. The sensitivity of a LPFG sensor to the applied strain and temperature increases with the order of LP modes when $j < 12$ (Shu *et al*. 2002). By utilizing two LPFG sensors in different cladding modes, the measured strain and temperature can be discriminated.

In this study, the CO_2 laser aided grating technique (Huang *et al*. 2013) was used to fabricate LPFG sensors on single-mode optical fibers (Corning SMF28e+). For a LPFG sensor, higher LP modes requires shorter grating period. Therefore, the spatial resolution of the CO_2 laser governs the maximum LP modes that can be fabricated. The width of the laser beam used in the study is approximately 90 μm. However, due to the heat transfer process, the heat affected zone on the fiber core is longer than 90 μm, thus the spatial resolution of the laser is compromised. The experimental results show that the maximum LP mode can be achieved is LP_{07} with a grating period of approximately 300 μm. Therefore, LP_{06} and LP_{07} modes of LPFG sensors were chosen and fabricated in this work by adjusting the grating period. The fabrication process was the same as the previous work (Guo *et al*. 2019). Specifically, LPFG sensors in LP_{06} mode with a grating period of 353 ± 0.1 μm and LPFG sensors in LP_{07} mode with a grating period of 301 ± 0.1 μm were fabricated, both having a resonant wavelength of 1550 nm. The total sensor length is approximately 4 cm.

2.2 Fe-C coated LPFG sensor for corrosion induced mass loss measurement

The evanescent field surrounding a LPFG sensor due to energy dissipation decays exponentially with the distance from the fiber surface in micron level. For corrosion monitoring, a thin coating layer on the sensor surface is required to cover most of the evanescent field and have the same chemical component ratio as the steel. In this study, Fe-C coating is prepared in approximately 6 cm length and placed on the surface of a LPFG corrosion sensor (Huang *et al*. 2013). A transparent yet conductive graphene/silver nanowire (Gr/AgNW) film was first coated on the LP_{06} mode LPFG sensor (Kim *et al*. 2017, Lee *et al*. 2013). The surface metallized LPFG was then connected to a negative electrode of the DC power supply and immersed in the electroplating solution (40 g/L $FeSO_4 \cdot 7H_2O$, 3.0 g/L L-ascorbic acid and 1.2 g/L citric acid). Another graphite rod was connected to the positive electrode to form an electrical circuit loop. The electroplating process was carried out at 5 mA current for 1.5 hours to form a 30 μm thick Fe-C layer on the LPFG surface. The fabricated sensor was then calibrated using electrochemical impedance spectroscopy (EIS) tests to establish the correlation between the mass loss of the Fe-C layer and the change in resonant wavelength (Chen *et al*. 2016, Huang *et al*. 2013).

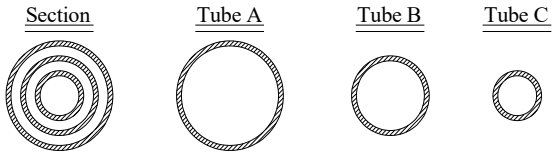

Fig. 1 Cross section of three steel tubes

Table 1 Dimension of the three types of tubes

Type	Tube A	Tube B	Tube C
OD (mm)	5.5	4.0	2.5
ID (mm)	5.0	3.5	2.0
Thickness (mm)	0.25	0.25	0.25
Length (cm)	5.0	5.0	5.0

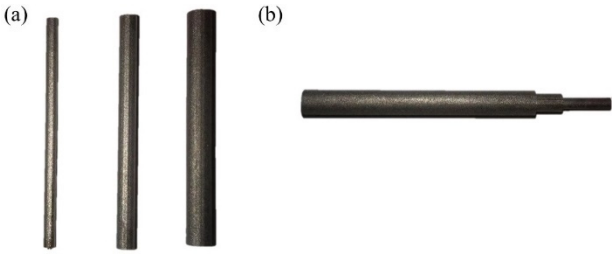

Fig. 2 Long-term corrosion threshold monitoring system from (a) three extracted tubes from steel rebar and (b) final arrangement of the tubes

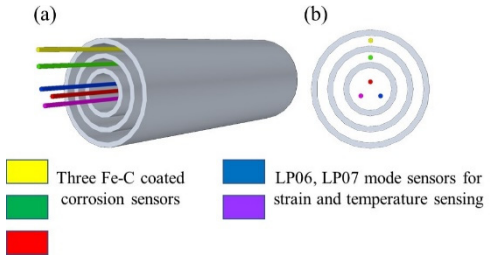

Fig. 3 Schematic view of an integrated sensing system: (a) three-dimensional view and (b) cross-sectional view

2.3 LPFG sensor integration and packaging

To protect fragile LPFG sensors and extend their service life for long-term corrosion monitoring, an integrated sensing system is proposed and designed. As shown in Fig. 1, three steel tubes, A, B and C, with different diameters are designed and arranged in a coaxial pattern. The outside diameter (OD), inside diameter (ID), thickness and length of the three tubes are listed in Table 1.

The three tubes were extracted from a piece of steel rebar through electrical discharge machining (EDM). Fig. 2 shows three extracted steel tubes and the finishing product of the three tubes in a coaxial arrangement by placing a small tube inside another large one.

As shown in Fig. 3, three Fe-C coated LPFG corrosion sensors in yellow, green and red colours were placed inside

the three steel tubes, respectively, for mass loss measurement. Two bare LPFG sensors in LP_{06} and LP_{07} modes, respectively, in blue and pink colours were deployed inside the inner tube for strain and temperature measurement. Two ends of the steel tubes were sealed using marine epoxy. The temperature and strain can be used to compensate the mass loss measurement.

3. Temperature sensing calibration

For temperature calibration, two LPFG sensors in LP_{06} and LP_{07} modes, respectively, were fixed on a short piece of steel rebar through epoxy and immersed in the water bath as shown in Fig. 4. During the calibration tests, a temperature profile started from the room temperature (25°C) to 75°C with a step of 10°C. The resonant wavelength shifts of the two sensors were measured through a high-speed optical interrogator (Micron Optics Si255). Fig. 5 presents the wavelength shift as a function of the temperature increase in each sensor.

Therefore, the correlation equation between the resonant wavelength and the temperature can be expressed into

$$\begin{aligned} \Delta\lambda_{06} &= 0.097\Delta T, \quad R^2 = 0.95 \\ \Delta\lambda_{07} &= 0.152\Delta T, \quad R^2 = 0.99 \end{aligned} \tag{2}$$

The sensitivity of the LP_{07} mode is approximately 1.57 times higher than that of the LP_{06} mode. For concrete structures, the temperature around rebar can rise to 70°C during concrete casting and hardening caused by the hydration heat. Once this process is complete, the temperature will drop to the ambient temperature. Therefore, a LPFG sensor can be used to monitor the change in early-age temperature in concrete. For steel structures, the temperature change usually comes from daily and seasonal changes in the surrounding environment.

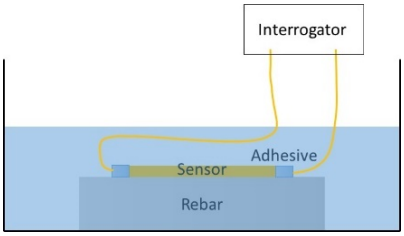

Fig. 4 Test setup for temperature sensing calibration

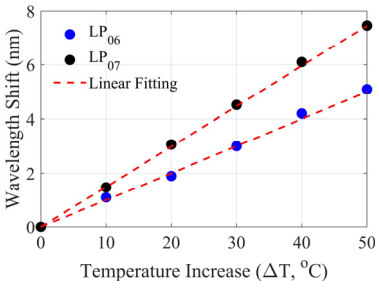

Fig. 5 Resonant wavelength shift of LP_{06} and LP_{07} sensors versus temperature increase

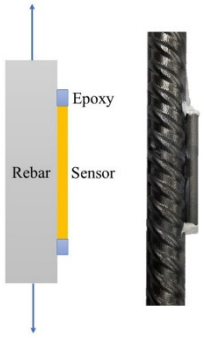

Fig. 6 Schematic illustration of the strain sensing setup

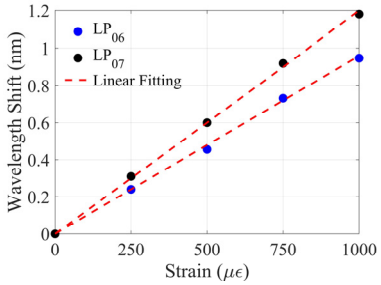

Fig. 7 Resonant wavelength shift of LP_{06} and LP_{07} sensors versus temperature increase

4. Strain sensing calibration

For strain calibration tests, the LP_{06} and LP_{07} modes LPFG sensors were fixed on the rebar with epoxy, which is then griped on a load frame as illustrated in Fig. 6. A total strain of 1000 με was applied on the rebar specimen with a step of 250 με. The shift in resonant wavelength corresponding to the applied strain is presented in Fig. 7. The correlation equation between the resonant wavelength and the applied strain is

$$\begin{aligned} \Delta\lambda_{06} &= 961.2\varepsilon, \quad R^2 = 0.97 \\ \Delta\lambda_{07} &= 1223.4\varepsilon, \quad R^2 = 0.98 \end{aligned} \tag{3}$$

in which the LP_{07} mode is about 1.27 times more sensitive than the LP_{06} mode. Since the LPFG sensor with a steel tube is fixed with the rebar using epoxy, the strain transfer rate highly depends on the bonding strength and stiffness between two components in contact. If other bonding method is used, the correlation equation between the increasing strain and the resonant wavelength shift must be re-calibrated.

5. Simultaneous measurement of strain and temperature

Two LP_{06} and LP_{07} LPFG sensors can be combined to discriminate the applied strain and temperature due to their different sensitivity coefficients. To illustrate this point, each sensor was deployed as shown in Fig. 8 in a high temperature furnace with its left end moved and controlled by a micrometer, and its right end fixed on a frame. The

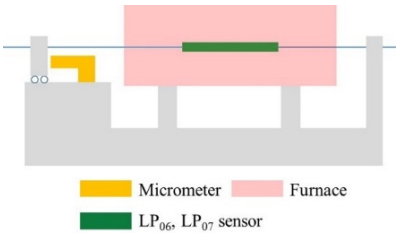

Fig. 8 Test setup for simultaneous strain and temperature measurement

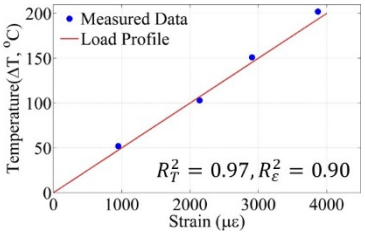

Fig. 9 Comparison of the sensor data with the thermal and loading profile

Table 2 Comparison of the applied and measured strain and temperature

Applied ΔT (°C)	Measured ΔT (°C)	Error	Applied strain ε (με)	Measured strain ε (με)	Error
50	52	4.0%	1000	962	3.8%
100	101	1.0%	2000	2164	8.2%
150	148	1.3%	3000	2869	4.4%
200	203	1.5%	4000	3750	6.3%

temperature in the furnace was increased from 50°C to 250°C at a step of 50°C. The strain applied on the LPFG sensor was from 0 to 4000 με with a step of 1000 με.

The measured strain and temperature were decoupled from the LP_{06} and LP_{07} mode wavelength shift using the following equation

$$\begin{Bmatrix} \Delta T \\ \varepsilon \end{Bmatrix} = \begin{Bmatrix} \alpha_{06} & k_{06} \\ \alpha_{07} & k_{07} \end{Bmatrix} \begin{Bmatrix} \Delta\lambda_{06} \\ \Delta\lambda_{07} \end{Bmatrix} \quad (4)$$

where α is the temperature sensitivity and k is the strain sensitivity. As shown in Fig. 9 and Table 2, the decoupled strain and temperature from the sensor measurements are in good agreement with the thermal and loading profiles. The maximum error is 4% in temperature and 8.2% in strain.

6. Corrosion induced mass loss monitoring

In an integrated sensing system of three steel tubes and three Fe-C coated LPFG sensors for corrosion monitoring of steel rebar in 3.5 wt.% NaCl solution, each steel tube can delay the exposure time of its protected Fe-C coated LPFG sensor to a specific pitting corrosion threshold of penetrating through the wall of that tube in years or decades. As the NaCl solution flows through the deteriorated tube and inundates the inside LPFG sensor, the corrosion rate immediately after the pitting corrosion threshold level or mass loss in the Fe-C layer can be measured. By combining the three tubes with the three Fe-C coated LPFG sensors, the integrated sensing system can be used to measure three critical corrosion thresholds in long term and their respective mass loss rates in short term, enabling the life-cycle monitoring and assessment of steel structures. Since the natural corrosion process takes months or even years to complete, accelerated corrosion tests are conducted to demonstrate the life-cycle assessment process of steel rebar by controlling the density of corrosion current.

6.1 Long-term mass loss correlation

The mass losses of a steel-tube sample and a rebar specimen are correlated when both are immersed in 3.5 wt.% NaCl solution during accelerated corrosion tests. Three arrangements of steel tubes were tested: a single tube A, a double tube A+B and a triple tube A+B+C. Each tube sample was sealed with marine epoxy at both ends and taped on a rebar specimen with 16 mm in diameter. To investigate its effect, the length of a tube sample and its supporting rebar specimen was considered to be 5 cm, 10 cm or 15 cm. Each of a combination of three tube samples and three tube lengths was tested under a current density of 500, 400 or 300 μA/cm^2, totalling 27 tube samples attached on 27 rebar specimens. The residual masses of the rebar specimen and the tube sample were measured every 24 hours using an electronic scale. A bare LPFG was placed inside the most inner tube to monitor the total penetration time of the tube walls. Corresponding to the mass loss measurement, the resonant wavelength of the bare LPFG sensor was monitored. Once shifted, the resonant wavelength indicated that the steel tubes outside the sensor had been fully penetrated, and the corrosion test was terminated.

Fig. 10 shows a tube sample attached to a rebar specimen prior to corrosion tests, the corroded rebar, the corroded single-tube sample, and the corroded double-tube sample with fully penetrated pitting corrosion at the end of accelerated tests. The mass losses of the rebar and the tubes are compared in Table 3 for all 27 test cases under various current densities. The mass loss rates of the rebar and the tube samples change little with the tube length. This is because a longer rebar specimen requires a larger current to keep a target current density, leading to the same current density through the steel tube.

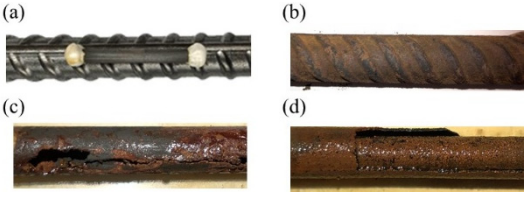

Fig. 10 (a) Steel tubes fixed on rebar; (b) corroded rebar; (c) corroded single steel tube; and (d) corroded double tubes

Table 3 Mass loss rate of the steel rebar and tubes under various current densities

Sample	Current density ($\mu A/cm^2$)	Rebar mass loss (%/day)			Steel tube mass loss (%/day)		
		5 cm	10 cm	15 cm	5 cm	10 cm	15 cm
Single Tube	300	0.24	0.26	0.26	1.9	2.1	1.9
	400	0.33	0.35	0.32	2.6	2.7	2.5
	500	0.43	0.44	0.41	3.3	3.4	3.5
Double Tubes	300	0.21	0.22	0.27	1.2	1.3	1.1
	400	0.35	0.37	0.39	1.5	1.6	1.7
	500	0.46	0.42	0.47	2.1	2.0	2.2
Triple Tubes	300	0.21	0.25	0.28	1.0	0.9	1.0
	400	0.30	0.37	0.35	1.3	1.3	1.2
	500	0.41	0.46	0.47	1.6	1.5	1.6

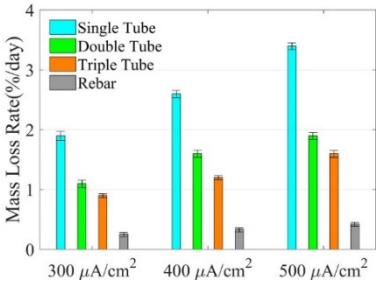

Fig. 11 Mass loss rates of the steel rebar and tubes under various current densities

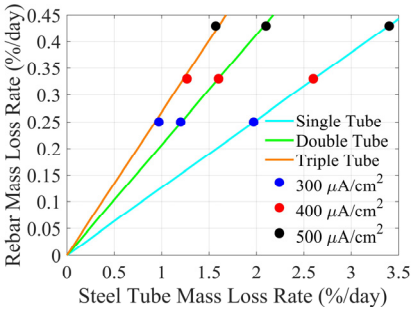

Fig. 12 Correlation of the mass loss rates between the rebar and steel tube

Therefore, the test results of three tube samples and the test results of nine rebar specimens of different lengths are averaged under each current density. The average value ± one standard deviation of each group is presented in Fig. 11. The data variation in each group of rebar specimens and tube samples is small, indicating consistent test results. The mass loss rate substantially decreases with the increasing number of steel tubes due to the increased total mass. The difference among the three tube arrangements becomes more significant as the current density applied on the tubes increases due to the accumulated effects over time.

Fig. 12 shows the linear correlation curve of the mass loss rates between the rebar and each steel tube arrangement. The linearity is independent of the current density applied during corrosion tests, and can thus be used to predict the mass loss of the rebar from the measurement of tube mass loss in various applications. The slope of the correlation curve changes with the type of tube arrangements. Let β_r, β_1, β_2, and β_3 be the mass loss rates of the rebar specimens, the single-tube samples, the double-tube samples, and the triple-tube samples, respectively. The mass loss rate of the rebar (β_r) can be related to the mass loss rate of each steel tube arrangement by

$$\begin{aligned} \beta_r &= \frac{\beta_1}{7.91}, \quad R^2 = 0.99 \\ \beta_r &= \frac{\beta_2}{4.84}, \quad R^2 = 0.97 \\ \beta_r &= \frac{\beta_3}{3.73}, \quad R^2 = 0.93 \end{aligned} \tag{5}$$

Once the mass loss rate of the steel tube (β_1, β_2, or β_3) is obtained from the integrated sensing system, the mass loss (η_r) of the rebar over time (t) can be derived under a constant corrosion current density by

$$\eta_r = \beta_r \cdot t \tag{6}$$

6.2 Penetration time of the steel tubes

For long-term corrosion monitoring, it is important to understand how long it takes for the steel tubes wall to be fully penetrated. This parameter determines the service life of the sensing system and is critical for sensor design. Table 4 lists the penetration time of each tube arrangement monitored by the inside bare LPFG sensor under various current densities. The penetration time through the wall of tube(s) decreases with the increasing current density due to the accelerated mass loss rate. The more the number of tubes, the longer time it takes for full penetration of the tube walls. However, the total penetration time through the walls of all tubes is not proportional to the number of tubes since the mass loss of the outer tube, once breached locally, will continue consuming current, leaving a reduced current density applied on the inner tube.

At the conclusion of corrosion tests, the total mass losses of each tube arrangement and the rebar were measured. They were also calculated by multiplying the penetration time and its corresponding mass loss rate. As shown in Table 5, the calculated mass loss rates of the tubes

Table 4 Penetration time of each tube sample under various current densities

Sample	Penetration time (Days)		
	300 μA/cm^2	400 μA/cm^2	500 μA/cm^2
Single tube	12	9	7
Double tubes	27	21	16
Triple tubes	46	35	29

and rebar are in good agreement with their respective test data with a maximum error of 7.7% for steel tubes and 9.7% for steel rebar. For each tube arrangement, the total mass losses of the tubes and the rebar change little with the applied current density. As indicated by Fig. 12, the mass loss of steel tubes normalized by their original mass decreases with the number of tubes due to the reduced current effect on the inner tube by its outer tubes. On the other hand, the mass loss of the rebar increases with the number of tubes out of proportion due to the nonlinear increase of penetration time as shown in Table 4.

6.3 Mass loss of inner tube after the pitting penetration of its outer tube

Since the penetration time of an inner tube in double-tube and triple-tube samples is longer than that in a single-tube sample, the corrosion process of the inner tube after the penetration of its outer tube warrants further examination. To simulate the corrosion process of an inner Tube B after the pitting penetration of an outer Tube A, the Tube B sealed at both ends with marine epoxy was connected to the positive electrode of the DC power supply and then inserted into the Tube A with open ends. The accelerated corrosion test was conducted as done in the previous section with 300, 400, and 500 μA/cm^2. The mass loss of Tube B was measured every 24 hours. At the same time, a single Tube B was tested and measured using the same current density for comparison. Table 6 compares the corrosion rates and penetration time of the single Tube B and the Tube B inside the Tube A under various current densities. The corrosion rate of the single Tube B was just the same as previously presented in Table 3 and Fig. 11. However, for the Tube B inside the Tube A, its corrosion rate was less than that of the single Tube B by 38%, 40% and 44% under 300, 400, and 500 μA/cm^2 current densities, respectively. Correspondingly, the penetration time of the Tube B in the Tube A is 58%, 67% and 71% longer than the single Tube B under the three current densities.

To understand the effect of the Tube A on both corrosion rate and penetration time of the inner Tube B, the circuit models of the single Tube B and the Tube B inside the Tube A are established as shown in Figs. 13(a) and (b). In these models, R_A and R_B are resistances of the Tube A and the Tube B, respectively, R_S is the solution resistance, and R_C is the contact resistance between the two tubes. For the single Tube B, the current in the Tube B (I_B) is equal to the applied current (I). For the Tube B inside the Tube A as shown in Fig. 13(b), although not directly wired to the electric circuit with the applied current, the outer Tube A is electrically in parallel with the inner Tube B though the conductive electrolyte with a contact resistance of R_C. In this case, the current in the Tube B can be derived and expressed into

$$I_B = \frac{R_A + R_S + R_C}{R_A + R_B + R_C + 2R_S} I \tag{7}$$

As a result, the actual current going through the inner Tube B is lower and the corrosion rate in the Tube B are thus reduced in comparison with the case without presence of the Tube A. Correspondingly, the penetration time through the wall of the inner Tube B is longer when the Tube A is present.

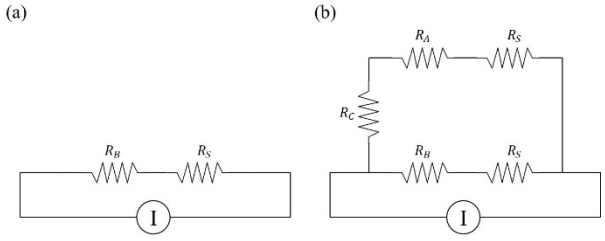

Fig. 13 Circuit model of (a) a single Tube B; and (b) the Tube B inside a Tube A

Table 5 Total mass loss of rebar and steel tube after penetration

Sample	Current density (μA/cm^2)	Steel tube mass loss (%)		Error	Rebar mass loss (%)		Error
		Measured	Calculated		Measured	Calculated	
Single Tube	300	24.1	23.6	2.1%	3.2	3.0	6.3%
	400	24.5	23.4	4.5%	3.1	2.9	6.5%
	500	25.7	23.8	7.4%	2.8	3.0	7.1%
Double Tubes	300	35.1	32.4	7.7%	6.3	6.7	6.3%
	400	35.3	33.5	5.1%	6.5	7.0	7.7%
	500	32.4	33.6	3.7%	6.2	6.8	9.7%
Triple Tubes	300	46.5	44.5	4.3%	11.9	11.3	5.0%
	400	46.9	44.3	5.5%	12.4	11.7	5.6%
	500	42.1	43.9	4.3%	11.3	11.9	5.3%

Table 6 Comparison on corrosion rate and penetration time of single Tube B and Tube B in Tube A

Current density ($\mu A/cm^2$)	Corrosion rate (%/day)		Penetration time (day)	
	Single Tube B	Tube B in Tube A	Single Tube B	Tube B in Tube A
300	2.1	1.3	12	19
400	2.5	1.5	9	15
500	3.4	1.9	7	12

6.4 Validation test of the integrated sensing system

The calibration tests and results of Fe-C coated LPFG corrosion sensors in 3.5 wt.% NaCl solution were reported under various strain levels (Guo *et al*. 2020). In Section 6.1, the mass loss of packaging steel tubes to protect the Fe-C coated LPFG sensors is well correlated with that of the steel rebar. The next step is to validate the service life, accuracy, and reliability of the sensing system. As shown in Fig. 14, three Fe-C coated LPFG sensors (LPFG 1, LPFG 2 and LPFG 3) were deployed inside each steel tube. The two ends of both the sensors and the tubes were sealed with marine epoxy. During corrosion tests in 3.5 wt.% NaCl solution, the sensing system was detached from the rebar every 24 hours so that the rebar mass loss can be weighed on an electronic scale. The corrosion test of the sensing system was terminated when the change in resonant wavelength of the inner LPFG 3 ceased.

During the accelerated corrosion tests, two types of current density profiles were applied. To simulate a stable corrosion environment, a constant current density of 500 $\mu A/cm^2$ was applied on the sensing system until all three tubes and all the Fe-C layers were penetrated completely. To simulate a changing corrosion circumstance, 300 $\mu A/cm^2$ was first applied on the sensing system until the Tube A and the Fe-C layer on the LPFG 1 sensor were completely penetrated as indicated by the stabilized resonant wavelength of LPFG 1. Then, 400 $\mu A/cm^2$ was applied until the Tube B and the Fe-C layer on the LPFG 2 sensor were corroded away. Finally, 500 $\mu A/cm^2$ was applied until the Tube C and the Fe-C layer of the LPFG 3 sensor were penetrated completely. Transmission spectra of the LPFG sensors were recorded every two hours. Once the wall of an outer steel tube was penetrated, the immediately inner Fe-C coated LPFG corrosion sensor started to measure the mass loss rate corresponding to a corrosion threshold of the outer wall penetration.

6.4.1 Under a constant current density (500 $\mu A/cm^2$)

Fig. 15 shows the accumulated resonant wavelength shift of the three sensors (LPFG 1, LPFG 2 and LPFG 3) over time. The sensing system clearly indicated three stages of corrosion. Right before the penetration of each tube, its immediate inner LPFG sensor has no wavelength shift. After the penetration, the LPFG sensor started to show a wavelength change in about two days. The penetration times of the three steel tubes are at 7, 16 and 29 days, respectively.

For the outer Tube A, the total average mass loss at penetration is 25.7% from the previous penetration test (Table 5). Since the current density is constant, the average mass loss rate can be calculated by dividing the total mass loss by the penetration time, which is 3.7% per day. The mass loss rate of the rebar can be obtained using Eq. (5). Thus, the total mass loss of the rebar can be estimated by multiplying its mass loss rate and penetration time. A similar procedure can be applied to the penetration of Tubes B and C by using the total mass loss of the double-tube sample and the triple-tube sample from the correlation results. The estimated and measured mass losses and associated loss rates of the rebar at each tube penetration are compared in Table 7. The estimated mass loss and rate are accurate with a maximum error of 8.8%.

The shift in resonant wavelength can be determined from a series of the transmission spectra of each LPFG corrosion sensor taken over time. As shown in Fig. 16, the relation between the wavelength shift and time is linear as consistently observed from all three LPFG sensors. The service life of each sensor was reduced from 46 hours (Guo *et al*. 2019) to about 16 hours due to the application of 500 $\mu A/cm^2$ current density. In combination with the calibration curve between the wavelength shift and mass loss of the Fe-C layer (Guo *et al*. 2019), the mass loss of the Fe-C layer over time can be derived. Since the total corrosion time of each sensor was 16 hours, the average mass loss rate of each Fe-C layer was about 6.3% per hour.

6.4.2 Under varying current densities over time

Fig. 17 shows the accumulated resonant wavelength shift of the three LPFG corrosion sensors over the life cycle of the sensing system under a varying current density. The

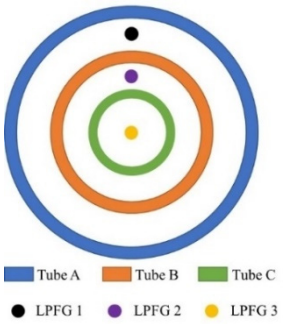

Fig. 14 Cross section of the sensing system

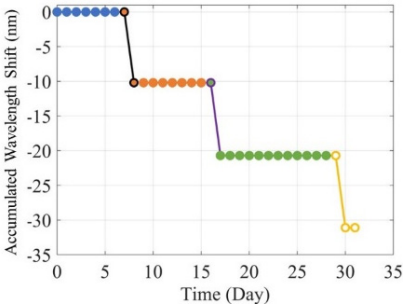

Fig. 15 Accumulated resonant wavelength shift over time under a constant current density

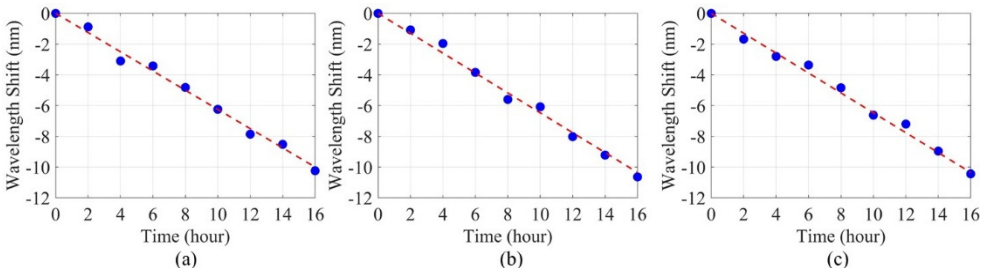

Fig. 16 Resonant wavelength shifts of (a) LPFG 1; (b) LPFG 2; and (c) LPFG 3 sensors over time under a constant current density (500 μA/cm^2)

Table 7 The estimated and measured mass losses and rates of the rebar under a constant current density

Penetration of tube	Mass loss rate (%/day)		Error	Mass koss (%)		Error
	Estimated	Measured		Estimated	Measured	
A	0.46	0.48	4.2%	3.1	3.4	8.8%
B	0.43	0.46	6.5%	6.9	7.4	6.8%
C	0.42	0.46	8.7%	12.2	13.3	8.3%

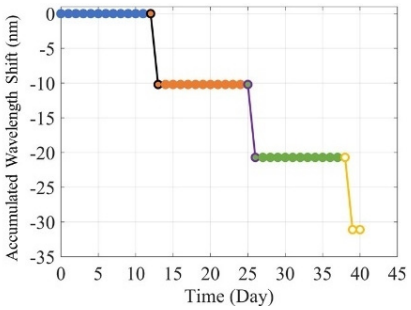

Fig. 17 Accumulated resonant wavelength shift over time under a varying current density

Table 8 Estimated and measured mass losses of the rebar under a time-varying current density

Penetration of tube	Rebar mass loss (%)		Error
	Estimated	Measured	
A	3.0	3.3	9.1%
B	6.3	6.8	7.4%
C	11.9	11.2	6.3%

Table 9 Average mass loss rate of the Fe-C layer

Sensor	LPFG 1	LPFG 2	LPFG 3
Mass loss rate (%/hour)	4.2	5.0	5.6

three tubes were penetrated at 12, 25 and 38 days, respectively. Since the current density is not constant, the mass loss rate of tubes may not be obtained accurately in order to estimate the rebar mass loss. However, the total mass loss of the rebar can still be estimated from the correlation test results since at the penetration time of each tube, the total mass loss of the rebar was not affected by the current density and remained at the same level. As listed in Table 8, the estimation is in good agreement with the measured mass loss with a maximum error of 9.1%.

Similar to the constant current density test, the resonant wavelength shift of each LPFG sensor can be obtained over time, as shown in Fig. 18. Once again, the wavelength shift increases linearly with the test time before the Fe-C layer is corroded completely. The service lives of the three sensors were about 24, 20 and 18 hours due to variation of the current density. The average mass loss rate of each Fe-C layer is listed in Table 9. The increased rate from LPFG 1

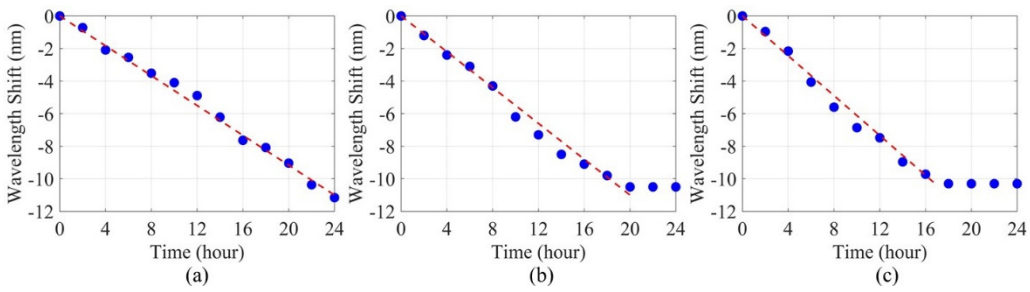

Fig. 18 Resonant wavelength shifts of (a) LPFG 1; (b) LPFG 2; and (c) LPFG 3 sensors over time under a varying current density from 300 μA/cm^2 to 500 μA/cm^2

to LPFG 3 implies the increasing of the applied current density.

7. Conclusions

In this study, an integrated sensing system of three steel tubes extracted from rebar, three Fe-C coated LPFG sensors in LP_{06} mode, and two LPFG sensors in LP_{06} and LP_{07} modes is designed and characterized for life-cycle monitoring of the rebar with strain and temperature compensation. Based on the test data and analysis, several conclusions can be drawn:

- Two LPFG sensors in LP_{06} and LP_{07} modes can be used together for simultaneous measurement of strain and temperature with high accuracy since they have dissimilar sensitivity coefficients. The maximum measurement error is 4.0% in temperature and 8.2% in strain.
- The mass losses of the steel tube and the rebar are correlated well, independent of test conditions (current density and tube length). The mass loss of the steel rebar estimated from the correlation equation is accurate with a maximum error of 9.7%.
- Under a constant current density, the mass loss rate of the rebar can also be derived accurately from the mass loss rate of the steel tube using the regression equation with less than 8.7% error. Under a time-varying current density, the mass loss rate of the rebar may not be obtainable from the equation since the penetration time of each tube differs from the penetration time taken during the correlation tests. In this case, the Fe-C coated LPFG sensor can provide the changing condition in corrosion current density through the measurement of Fe-C mass loss rate.
- For three coaxial steel tubes with identical wall thickness, the pitting corrosion penetration time of the inner tube is appreciably longer than that of the outer tube. This is because the presence of the outer tube reduces the current density applied on the inner tube. Under a current density of 500 $\mu A/cm^2$, the penetration time of the three coaxial steel tubes substantially increases to 29 days from the 2/3 days for the Fe-C layer on the LPFG sensor. The combination of the tube and Fe-C layer in the proposed sensing system enables both the long-term and short-term monitoring of corrosion in steel rebar.

Acknowledgments

This research was funded by the U.S. Department of Transportation, Office of the Assistant Secretary for Research and Technology (USDOT/OST-R), under Grant No. 69A3551747126, through the INSPIRE University Transportation Center at Missouri University of Science and Technology. The views, opinions, findings and conclusions reflected in this publication are solely those of the authors and do not represent the official policy or position of the USDOT/OST-R, or any State or other entity. Thanks are also due to the Chinese Scholarship Council (CSC) to provide the scholarship to the first author during his PhD study.

References

Bao, Y. and Chen, G. (2016), "High-temperature measurement with Brillouin optical time domain analysis of an annealed fused-silica single-mode fiber", *Optics Lett*., **41**(14), 3177-3180. https://doi.org/10.1364/ol.41.003177

Bhatia, V., Murphy, K.A., Claus, R.O., Jones, M.E., Grace, J.L., Tran, T.A. and Greene, J.A. (1996), "Optical fibre based absolute extrinsic Fabry-Perot interferometric sensing system", *Measure*. *Sci*. *Technol*., **7**(1), 58-61. https://doi.org/10.1088/0957-0233/7/1/008

Chen, Y., Tang, F., Bao, Y., Chen, G. and Tang, Y. (2015), "Corrosion monitoring of steel bar in mortar using Fe-C coated long-period fiber gratings", *NACE - International Corrosion Conference Series*, Dallas, TX, USA, January. https://doi.org/10.13140/RG.2.1.4756.2481

Chen, Y, Tang, F., Bao, Y., Tang, Y. and Chen, G. (2016), "A Fe-C coated long-period fiber grating sensor for corrosion-induced mass loss measurement", *Optics Lett*., **41**(10), 2306-2309. https://doi.org/10.1364/OL.41.002306

Deng, L. and Cai, C.S. (2007), "Applications of fiber optic sensors in civil engineering", *Struct*. *Eng*. *Mech*., *Int*. *J*., **25**(5), 577-596. https://doi.org/10.12989/sem.2007.25.5.577

Deng, L., Yan, W. and Nie, L. (2019), "A simple corrosion fatigue design method for bridges considering the coupled corrosion-overloading effect", *Eng*. *Struct*., **178**, 309-317. https://doi.org/10.1016/j.engstruct.2018.10.028

Erdogan, T. (1997), "Cladding-mode resonances in short-and long-period fiber grating filters", *JOSA A*, **14**(8), 1760-1773. https://doi.org/10.1364/JOSAA.14.001760

Figueira, R. (2017), "Electrochemical Sensors for Monitoring the Corrosion Conditions of Reinforced Concrete Structures: A Review", *Appl*. *Sci*., **7**(11), 1157. https://doi.org/10.3390/app7111157

Gloge, D. (1971), "Weakly guiding fibers", *Appl*. *Optics*, **10**(10), 2252-2258. https://doi.org/10.1364/AO.10.002252

Guo, C., Fan, L., Wu, C., Chen, G. and Li, W. (2019), "Ultrasensitive LPFG corrosion sensor with Fe-C coating electroplated on a Gr/AgNW film", *Sensors Actuat*. *B*: *Chemical*, **283**, 334-342. https://doi.org/10.1016/j.snb.2018.12.059

Guo, C, Fan, L. and Chen, G. (2020), "Corrosion-Induced Mass Loss Measurement under Strain Conditions through Gr/AgNW-Based, Fe-C Coated LPFG Sensors", *Sensors*, **20**(6), 1598. https://doi.org/https://doi.org/10.3390/s20061598

Huang, Y., Gao, Z., Chen, G. and Xiao, H. (2013), "Long period fiber grating sensors coated with nano iron/silica particles for corrosion monitoring", *Smart Mater*. *Struct*., **22**(7). https://doi.org/10.1088/0964-1726/22/7/075018

Kim, C.-L., Jung, C.-W., Oh, Y.-J. and Kim, D.-E. (2017), "A highly flexible transparent conductive electrode based on nanomaterials", *NPG Asia Mater*., **9**(10), 438. https://doi.org/10.1038/am.2017.177

Lee, D., Lee, H., Ahn, Y., Jeong, Y., Lee, D.-Y. and Lee, Y. (2013), "Highly stable and flexible silver nanowire–graphene hybrid transparent conducting electrodes for emerging optoelectronic devices", *Nanoscale*, **5**(17), 7750-7755. https://doi.org/10.1039/C3NR02320F

Leng, J. and Asundi, A. (2003), "Structural health monitoring of smart composite materials by using EFPI and FBG sensors", *Sensors Actuat*. *A*: *Phys*., **103**(3), 330-340. https://doi.org/10.1016/S0924-4247(02)00429-6

Mizuno, Y., Hayashi, N., Tanaka, H., Wada, Y. and Nakamura, K. (2015), "Brillouin scattering in multi-core optical fibers for sensing applications", *Scientif. Reports*, **5**, 1-9. https://doi.org/10.1038/srep11388

Panossian, Z., de Almeida, N.L., de Sousa, R.M.F., de Souza Pimenta, G. and Marques, L.B.S. (2012), "Corrosion of carbon steel pipes and tanks by concentrated sulfuric acid: a review", *Corrosion Sci*., **58**, 1-11. https://doi.org/10.1016/j.corsci.2012.01.025

Shu, X., Zhang, L. and Bennion, I. (2002), "Sensitivity characteristics of long-period fiber gratings", *J. Lightwave Technol*., **20**(2), 255-266. https://doi.org/10.1109/50.983240

Snyder, A.W. (1969), "Asymptotic expressions for eigenfunctions and eigenvalues of a dielectric or optical waveguide", *IEEE Transact. Microw. Theory Techniq*., **17**(12), 1130-1138. https://doi.org/10.1109/TMTT.1969.1127112

Urrutia, A., Goicoechea, J., Ricchiuti, A.L., Barrera, D., Sales, S. and Arregui, F.J. (2016), "Simultaneous measurement of humidity and temperature based on a partially coated optical fiber long period grating", *Sensors Actuat. B: Chem*., **227**, 135-141. https://doi.org/10.1016/j.snb.2015.12.031

Vengsarkar, A.M., Lemaire, P.J., Judkins, J.B., Bhatia, V., Erdogan, T. and Sipe, J.E. (1996), "Long-period fiber gratings as band-rejection filters", *J. Lightw. Technol*., **14**(1), 58-64. https://doi.org/10.1109/50.476137

Wang, J., Dong, B., Lally, E., Gong, J., Han, M. and Wang, A. (2010), "Multiplexed high temperature sensing with sapphire fiber air gap-based extrinsic Fabry–Perot interferometers", *Optics Lett*., **35**(5), 619-621. https://doi.org/10.1364/OL.35.000619

Wen, X., Ning, T., Bai, Y., Li, C., Li, J. and Zhang, C. (2015), "Ultrasensitive temperature fiber sensor based on Fabry-Pérot interferometer assisted with iron V-groove", *Optics Express*, **23**(9), 11526-11536. https://doi.org/10.1364/OE.23.011526

Xu, F., Ren, D., Shi, X., Li, C., Lu, W., Lu, L. and Yu, B. (2012), "High-sensitivity Fabry–Perot interferometric pressure sensor based on a nanothick silver diaphragm", *Optics Lett*., **37**(2), 133-135. https://doi.org/10.1364/OL.37.000133

Zaki, A., Chai, H.K., Aggelis, D.G. and Alver, N. (2015), "Non-destructive evaluation for corrosion monitoring in concrete: A review and capability of acoustic emission technique", *Sensors*, **15**(8), 19069-19101. https://doi.org/10.3390/s150819069

Zhao, Y., Li, X.G., Zhou, X. and Zhang, Y.N. (2016), "Review on the graphene based optical fiber chemical and biological sensors", *Sensors Actuat. B: Chem*., **231**, 324-340. https://doi.org/10.1016/j.snb.2016.03.026.

HJ